ORIGINAL PAPER

Sedimentary and volcanic reconstruction in the Ngwa Basin along the "Cameroon Volcanic Line" (Dschang, West-Cameroon): facies analyses and petrology constraints

Milan Stafford Tchouatcha[1] · Cecile Olive Mbesse[2] · Abdalla Mousa El Ayyat[3] · Amr Said Deaf[3] · Pafouly Kassi Kassi[2]

Abstract

The Cenozoic Ngwa Basin is located along the Cameroon Volcanic Line (CVL) at the southern part of the Mount Bambouto slope. Collected samples from this basin have been studied to investigate the provenance, maturity, tectonic setting, and conditions of sedimentation via facies analyses, geochemical, petrographical, X-ray diffraction (XRD), and heavy minerals studies. The strata succession consists of alternation of positive and negative sequences with three facies association and height lithofacies (Gcm, Gmm, Gmi, Sm, Sh, Fm, Fh, and Fhfc lithofacies), interbedded with the volcanic rocks made up of rhyolite, ash pyroclasts and olivine basalt. Facies analyses show high variations in sedimentation conditions, with alternatively high and moderate to low energies of deposition influenced by climate and tectonics. Petrographic study of pebbles indicates the presence of varied volcanic rocks such as andesite, basalt, trachyte, dacite, and ignimbrite around the study area. Analysis of the major elements points to volcanic heterogeneous provenance of sediments, with dominance of mafic to intermediate igneous provenance, in the middle and upper part of deposits, and secondary recycled and felsic provenance in its lower part. The studied sediments are mature (index of compositional variability: ICV generally < 1) and show high recycling manner (chemical index of alteration: CIA 71.81 to 99.00 and plagioclase index of alteration: PIA 79.37 to 99.71). This recycled character is further confirmed by the presence of inclusively quartz pebbles in the lower part of the studied sequence and generally by the high $\sum$REE values (621.57 to 11,280.5 ppm > PAAS: 184.77 ppm). Sediments were deposited in swamping settings with prevailing oxic conditions (high to slight negative Ce anomalies: 0.19 to 98) under warm and semi-humide with periodically semi-arid to arid climate when one proceeds up-section as is evidenced by the major elements and XRD data. Sedimentation in the Ngwa Basin reflects a composite tectonic setting, which is probably connected to the Late Jurassic-Early Cretaceous Gondwanan continental rifting and the South Atlantic Ocean evolution. The cases of Cenozoic volcaniclastic deposits associated with terrigenous facies are reported in the Southern Apennines, Italy.

Keywords Sedimentation · Volcanism · Tectonics · Cameroon Volcanic Line · Dschang · West-Cameroon · Gondwana rifting

✉ Milan Stafford Tchouatcha
   inter_milanac@yahoo.fr

1 Department of Earth Sciences, University of Dschang, P.O. Box 67, Dschang, Cameroon

2 Department of Earth Sciences, University of Yaoundé I, P.O. Box 812, Yaounde, Cameroon

3 Department of Geology, Faculty of Science, Assiut University, Assiut 71516, Egypt

Introduction

The history of the CVL is related to the Gondwana continental rifting during the Late Jurassic to Early Cretaceous, the progressive separation of the South American and African plates, and the opening of the South Atlantic Ocean (Maurin and Guiraud 1993; Pletsch et al. 2001; Njike Ngaha et al. 2014). The evolution of South Atlantic Ocean has led both to the creation of magmatic massifs (Njonfang et al. 2011) and sedimentary basins (Njike Ngaha et al. 2014) in Cameroon. The mechanism of episodic emplacement of alkaline magmatism through the entire African continent, and especially along the CVL, can be better explained in terms of

complex interactions between hotspots and pre-Cambrian faults (Njonfang et al. 2011). The period between the magmatic events generally corresponds to more or less intense erosion phenomena and the formation of sedimentary basins as the case of Ngwa Basin located along the CVL.

Cameroon has two types of sedimentary basins, the intracontinental and coastal basins of Lower Cretaceous age. Several studies (e.g., Njike Ngaha 1984; Ndjeng 1992; Eyong 2003; Tchouatcha 2011) indicate that the sedimentary formations are generally covered by Cenozoic volcanic rocks, and some with Cenozoic to Recent volcaniclastic deposits (Bilobe et al. 2021; Tchouatcha et al. 2021a). The Ngwa Basin shows certain peculiarities with the sedimentary facies alternate with volcanic deposits (Bessong et al. 2017), and hence the characteristics of the volcano-sedimentary series designation, reported in the Southern Italia (Guerrera and Veneri 1989; Prosser et al. 2008).

The location of the Ngwa Basin in a slope of Mount Bambouto suggests that the later is the main sediment provider of the Ngwa depression. A few studies have been dealt with Ngwa Basin (Capponi 1945; Kenfack et al. 2011; Benammi et al. 2017; Bessong et al. 2017), however, the sediment provenance and facies analyses are still lacking and the new obtained data indicate that the sedimentary and volcanic facies are more diversified. In this work, we provide the detailed lithostratigraphic column and a new evidence for alternation between sedimentary and volcanic processes in the Ngwa Basin. Geochemistry and heavy mineral analyses have been used to investigate the source rock characteristics. Geochemical analyses for the fine-grained sediments are more useful to constraint geochemical signatures (Taylor and McLennan 1985), and heavy minerals for more coarse-grained sediments (Parfenoff et al. 1970) have been used to shed some light on the provenance. Petrographic analyses have been used to characterize the lithology of sedimentary and volcanic deposits. In addition, the environments and conditions of sedimentation have been inferred, based on the facies analyses alongside with geochemical analyses data.

Geological setting

The Ngwa sedimentary Basin (Fig. 1) is located on the southern flank of Bambouto volcano in the west region of Cameroon along the CVL and represents the third largest volcano of the CVL (Kagou Dongmo et al. 2001). The CVL is a 100-km-wide geological lineament, oriented N 130° E and characterized by an alignment of oceanic and continental volcanoes from Gulf of Guinea to the interior of African continent over 1600 km (Marzoli et al. 2000). The Mount Bambouto is the third largest volcano of the CVL after Mounts Cameroon and Manengouba with volcanic activity ranges from Miocene to Quaternary (Kagou Dongmo

et al. 2010). These structures are thought to be induced by a network of combined faults, related to an intra-plate sliding system of high extension (Deruelle et al. 1991). The geological history of Mount Bambouto is divided into four main stages from the Miocene to the Quaternary (Youmen et al. 2005; Kagou Dongmo et al. 2010). The first stage (21 Ma) was devoted to the building of the primitive shield volcano with alkaline basalts. The second stage (18.5–15.3 Ma) is the collapse of the Caldera in response to the draining of a large sub-volcanic evolved magma reservoir by ignimbritic rhyolites and trachytes. The third stage (15.1–4.5 Ma) renews with the basanites to mugearites effusive activities together with post-caldera extrusions of trachytes between 15 and 8.8 Ma, and of phonolites between 12.9 and 5.2 Ma. The fourth stage during the recent Quaternary is the northeastern upper flank basanite eruption.

The Ngwa Basin is a small depression and is regarded as one of the uncommon continental basins, which is characterized by the presence of lignite deposits (Capponi 1945). The ages of deposits of the Ngwa Basin have been proposed by the study of the lignite in this basin. Capponi (1945) suggested a Tertiary age for this lignite in comparison with lignite known from the southern part of Nigeria. Benammi et al. (2017) attributed an age between 20.04 and 20.21 Ma to the lignite from magneto-stratigraphical analyses and K–Ar dating. Bessong et al. (2017) proposed an age that ranges from the Late Eocene to the Early Miocene based on palynological recorded assemblages.
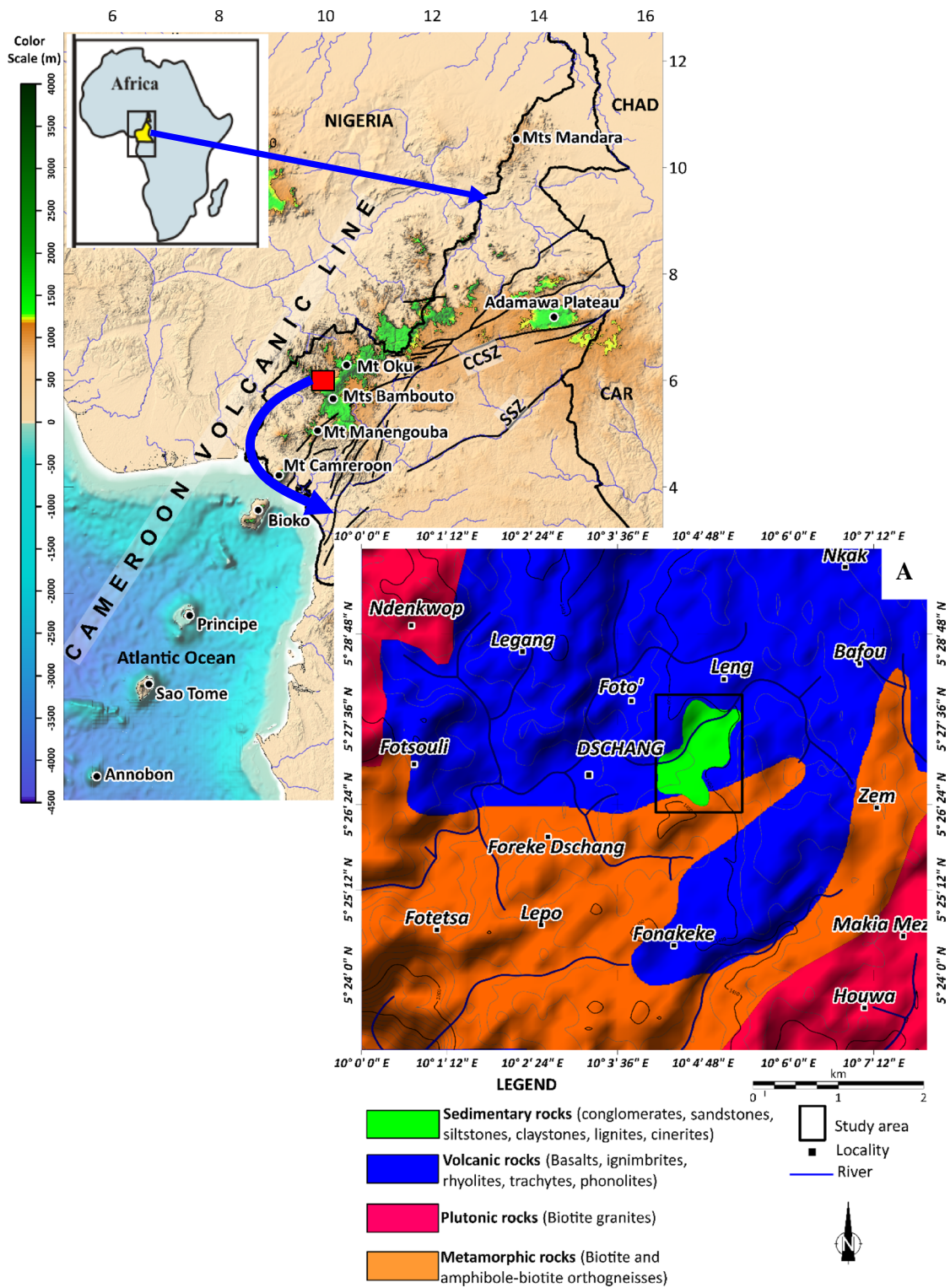
According to Kenfack et al. (2011), Benammi et al. (2017), and Bessong et al. (2017), the sedimentary succession in the Ngwa Basin is made up of volcano-clastic sediments. Sedimentary facies are conglomerates, sand/sandstones, and clays/claystones interbedded with cineritic and tuff/tuffite (Benammi et al. 2017; Bessong et al. 2017).

Methods of data base

To throw some light on the provenance and conditions of sedimentation in the Ngwa Basin, geochemical analyses for fine-grained rocks, petrographical investigations for pebbles with volcanic and sedimentary rocks, mineralogical analyses for fine-grained shales and claystones), and heavy mineral studies for coarse-grained rocks and facies analyses have been carefully performed.

Sixty polished thin sections have been prepared at Langfang Rock Detection Technology Services Ltd in Hebei (China) and in Assiut University (Egypt). The petrographic study of these samples has been carried out under polarized microscope at the Laboratory of Petrology and Structural Geology in the University of Yaoundé 1 (Cameroon).

The X-ray diffraction patterns of eleven representative samples (shales/claystones) have been obtained from a

Fig. 1 **A** Geological map of the Ngwa Basin (modified after Kwékam et al. (2015) and Fosing et al. (2019)). **B** Location of the study area in the Cameroon Volcanic Line map

Bruker D8-Avance Eco 1Kw diffractometer (Copper Kα radiance. $\lambda = 1.5418$ Å, $V = 40\ 125$ kV, $I = 25$ mA) with Lynxeye Xe energy-dispersive detector in the laboratory of "Argiles, Géochimie et Environments Sédimentaires

(AGES)" at the University of Liege, Belgium. The analyses have been carried out on the bulk material (non-oriented powder with grinded particles < 50 μm).

Ten thin sections were prepared at the University of Yaoundé 1 for heavy mineral analyses. The methods followed were those of Parfenoff et al. (1970). After washing and sieving the samples, the heavy minerals ($d > 2.89$) were extracted with the help of Bromoforme. The fraction retained is between 100 and 200 μm.

Whole-rock geochemical analyses of thirteen representative fine-grained samples have been carried out at Bureau Veritas Commodities, Vancouver, Canada. Prepared samples (homogenized powder) have been mixed with LiBO2/Li2B4O7 flux. Crucibles were fused in a furnace at 1000 °C. The cooled bead was dissolved in ACS grade nitric acid. Trace elements (including rare earth elements REE) were determined by the inductively coupled plasma mass spectrometry (ICP-MS). Major element oxides were obtained by inductively coupled plasma-atomic emission spectrometry (ICP-AES). Loss on ignition (LOI) was determined by igniting a sample split then measuring the weight loss. The assay uncertainties varied from 0.1 to 0.04% for major elements, 0.1 to 0.5% for trace elements, and 0.01 to 0.5 ppm for REE. Accuracy for REE is estimated at 5% for concentrations > 10 ppm and 10% when lower.

Results

Facies analyses

The deposits of the Ngwa Basin (Fig. 2) have been grouped into three major facies associations including conglomerate facies (Gmm, Gcm, and Gmi), sandstones facies (Sm and Sh), and claystones facies (Fm, Fh, and Fhfc). The different lithofacies in Table 1 have been described, interpreted, and classified. Furthermore, the facies code used was modified from that of Miall (1978, 1996).

Conglomerates facies

The conglomerate facies (Fig. 3A) comprises three lithofacies including (A) massive clast–supported conglomerates (Gcm), (B) massive matrix–supported conglomerates (Gmm), and (C) imbricated massive conglomerates (Gmi).

Massive clast-supported conglomerates (Gcm) The massive clast–supported conglomerates are heterolithic conglomerates with varied types of exclusively volcanic pebbles. This facies is poorly sorted, and the clasts are generally well rounded with sizes up to 0.15 m. The matrix is unconsolidated and consists of clayey sand facies (about 15–25%). There are sometimes lenticular clayey sand intercalations (0.15 m thick), which affected by overload pressure. The thickness ranges from 0.20 to 5 m. It is sometimes associated
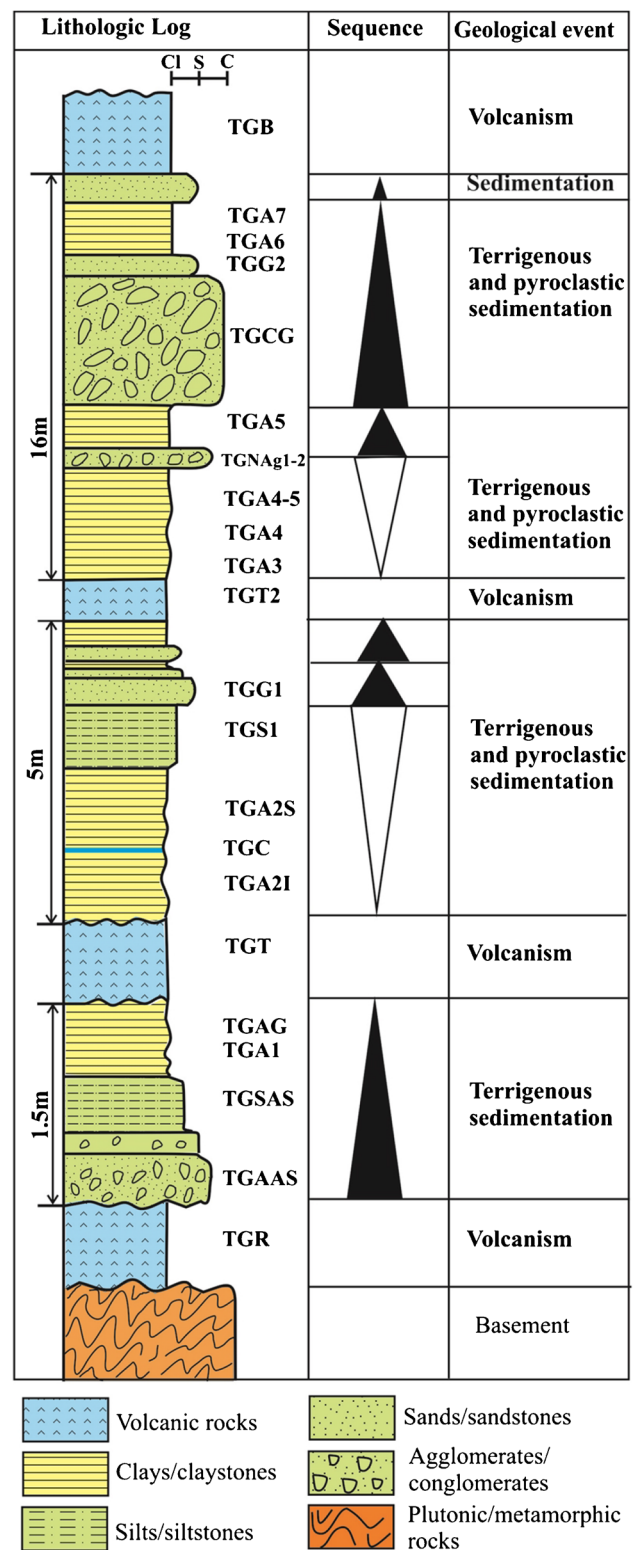

Fig. 2 Synthetic log of the Ngwa Basin showing alternation between volcanism and sedimentation. Abbreviations: Cl clay, S sand, Cg conglomerate

Table 1 Lithofacies of sediments from the Ngwa Basin. The facies codes are from Miall (1996) and Ntamak-Nida et al. (2010). The interpretations provided are according to Lowe (1982), Nilsen (1982), and Miall (1978, 1996)

Facies code	Facies name	Lithology	Structure	Depositional processes and environment
Gcm	Massive clast-supported conglomerates	Conglomerates, poorly sorted, rounded to sub-rounded volcanic pebbles, moderately to poorly consolidated, clayey sand matrix with 15 to 25% of total rock	Massive, slightly sharp basal boundary with sandstone, sharp upper boundary with clay / claystone, 0.2 to 5 m thick	Deposits from gravity flow in a steep topographic gradient (Nilsen 1982) with distal and proximal clasts or pebbles in swampy environment
Gmm	Massive matrix-supported conglomerates	Same like Gcm, but with 55 to 65% of clayey sand matrix	Same to Gcm with less than 1 m thick, pebbles flotting in the matrix	Plastic debris flow and steep topography (Nilsen 1982) swampy environment
Gmi	Imbricated massive conglomerates	Same to Gcm	Imbrication, less than 0.60 m thick of bed	Stream flow processes of bed load traction carpet (Nilsen 1982), high-energy deposits (Miall 1996)
Sm	Massive sandstones	Fine to coarse-grained sandstones, moderately to poorly sorted, angular with rare subrounded grain shapes, clayey matrix (25–30%), poorly consolidated	Massive, slightly sharp upper boundary with conglomerates, sharp basal boundary with claystones	Rapid deposition from turbulent suspension (Lowe 1982)
Sh	Horizontal layered sandstones	Fine-grained sandstones, moderately to well sorted, well to moderated consolidated	Lamination and bedding, sharp upper and basal boundaries, 0.10 to 0.15 m thick	Planar bed flow, shallow high velocity flows (Miall 1978)
Fh	Horizontal layered claystones	Claystones, grayish to gray dark, well sorted, moderately indurated	Lamination, sharp boundary with sandstones, erosive boundary with cinerites 0.10 to 4 m thick	Deposits from suspension (Miall 1996) and low energy in swampy environment
Fm	Massive claystones	Claystones, gray color moderately to poorly sorted	Massive with cracks, sharp boundary 0.3 to 0.70 m	Deposits from weak traction current (Miall 1996)
Fhfc	Horizontal layered claystones	Same to Fh, but with coal fragments and leafs	Lamination, sharp boundary with sandstones, erosive boundary with cinerites, 0.10 to 4 m thick	Same to Fh

Fig. 3 Field photographs and some facies. **A** Varied conglomerate lithofacies; **B** alternation of shale (Fl) and sandstone (Sl); **C** shale (Fl); **D** intercalation of volcanic rock (cinerite) between black shale (Fml); **E** compact sandy clay (Fm) with crack; **F** intercalation of sedimentary deposits (clay) between volcanic deposits (rhyolite and tuff); **G** leaf fossil preserved in the black shale (Fmlf)
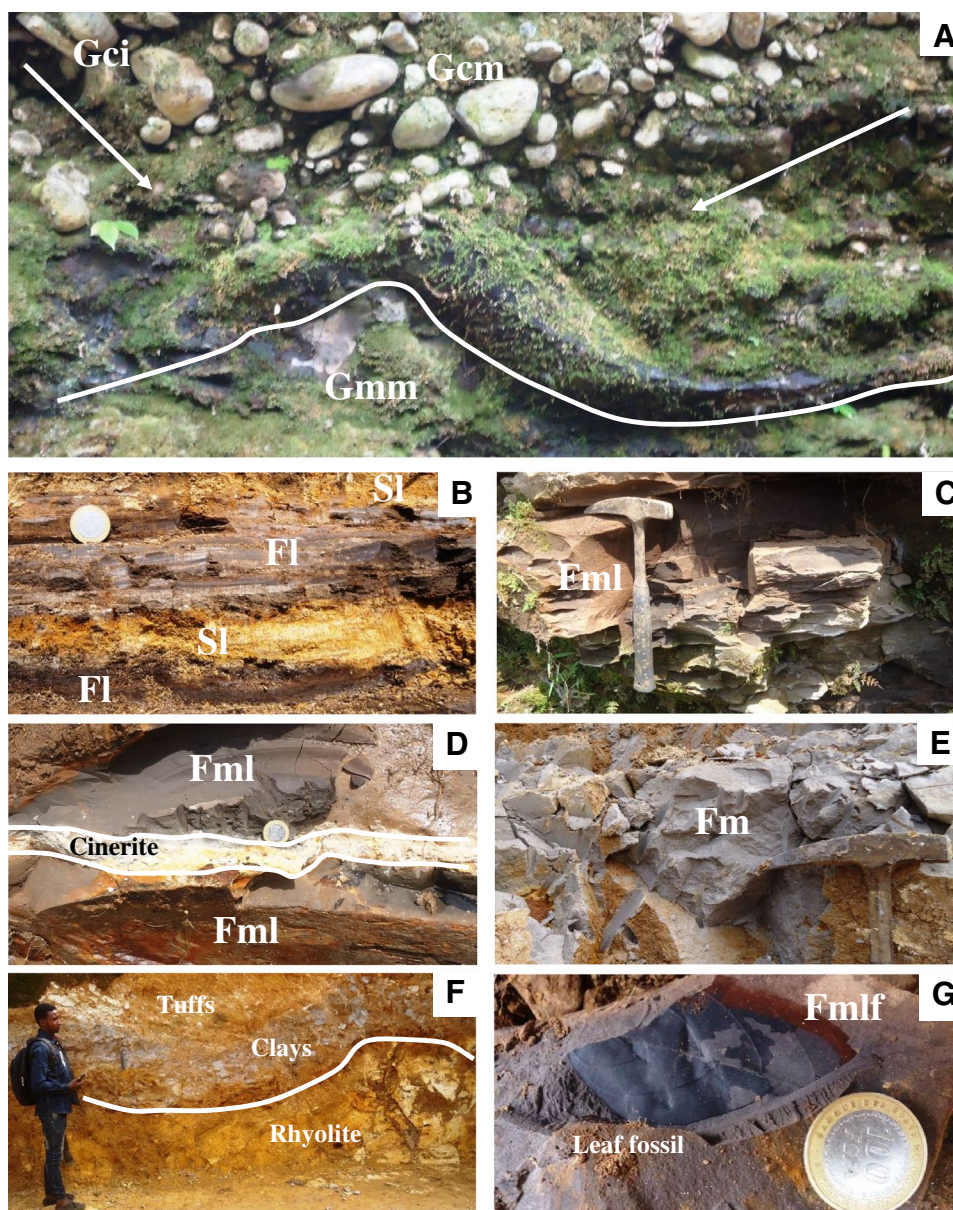
with Gmm and Gmi facies. The basal boundary with sandy facies is slightly sharp.

Imbricated massive conglomerates (Gmi) This lithofacies is associated with Gcm lithofacies. It is moderately to poorly sorted with clayey sand matrix and is massive clast-supported. The pebble is also well rounded with some rare sub-angular clasts. The imbricated pebbles display several water current trends (Fig. 3A). The thickness is generally less than 1 m.

Massive matrix-supported conglomerates (Gmm) This lithofacies is intercalated within the Gcm lithofacies. It is poorly sorted with rounded clasts associated with rare angular to sub-angular pebbles with 1 to 12 cm in size. The dominant

matrix (more 60% of the total rock) is clayey sand, which consists mainly of sub-angular to rounded sand grains. The thickness is less than 1 m.

Sandstones facies

The sandstone facies is made up of two lithofacies (A) the massive sandstones (Sm) and (B) the horizontal layered sandstones (Sh).

Massive sandstones (Sm) The massive sandstone lithofacies (Sm. TGG2) is moderately to poorly sorted, fine- to coarse-grained, angular with rare sub-rounded grain shapes, and its color is gray. The particle sizes range from 0.2 to 1.5 mm. It is composed of abundant feldspar made up of sanidine

essentially (40–50%). rock fragments (20–25%) made up of microlitic and spherolitic rocks, associated with rare quartz. The matrix is mainly clayey (25–30% of the total rock). The microstructure is medium to coarse clastic and hetero-granular. Its thickness ranges between 0.6 and 2 m with no internal structure. It alternates with conglomerates and clayey facies, and the boundaries are sharps.

Horizontal layered sandstones (Sh) The horizontal layered and laminated sandstones (Sh. TGG1) are moderately to well sorted, fine-grained, have very angular to angular grain-shapes, and yellowish color, which linked probably to the weak weathering. The particle sizes are generally ˂ 0.4 mm. They are composed of abundant undifferentiated quartz and feldspar (85–90%) associated with muscovite (2–3%). The matrix is ferruginous (10%), and the microstructure is fine clastic iso- to sub-hetero-granular. The thickness ranges from 0.10 to 0.15 m. This facies is marked by laminations and alternates with Fh (horizontal layered claystones) with more or less sharp boundaries (Fig. 3B).

Claystones facies

It consists of three lithofacies types: (A) horizontal layered claystones, (B) massive claystones/siltstones (Fm), and (C) massive claystones (Fm) and horizontal layered sandstones (Fh).

Horizontal layered claystones (Fh) The horizontal layered claystones (Fh) are moderately indurated, grayish to gray dark in color due to varied concentration of organic matter (Fig. 3C). The microstructure is very fine clastic and iso-granular. Generally, it is laminated and alternates with Sh and Fm lithofacies. Besides, it encloses thin layers of siltstones and is also associated with Fmlfc facies. The thickness ranges from 0.10 to 4 m. The contacts with cinerite (ash pyroclastic) deposit are erosive (Fig. 3D).

Massive claystones/siltstones (Fm) The massive claystones/siltstones (Fm) (Fig. 3E) are also moderately indurated, grayish to greenish gray in color with 0.30 to 0.70 m thick. They are sometimes sandy with scattered pebbles (cms long) and display desiccation cracks. The microstructure is fine clastic and hetero-granular. They alternate with Fh lithofacies. This facies includes sporadic leaf fossils and tiny fragments of coal. At the base, the boundary between this facies and rhyolite is erosive (Fig. 3F).

Horizontal layered claystone with plant fossils and coal (Fhfc) The horizontal layered claystone with fossils and coal (Fhfc) is always associated with Fh lithofacies, and they share the same features. Meanwhile, the Fhfc lithofacies contains abundant plant fossils as varied types of leafs (Fig. 3G). The plant leaf fossils are sometimes well preserved and associated with mm to cm coal fragments and rare fossilized fruits.

Petrographic analyses

The petrographic analyses include the study of pebble of conglomerates (TGCG), sedimentary facies and volcanic rocks (TGB. TGR and TGC) in the study area.

Petrographic analyses of pebbles

According to the petrographic analyses of the pebbles, at least six lithological types of these pebbles have been identified including ignimbrite, volcanic glass, rhyolite, breccias, basalt/andesine, and trachyte.

Ignimbrite Ignimbrites are gray dark to grayish with flame structure and phenocrysts (1–2%) of quartz and sanidine (less than 0.1 mm in size). The microlite is composed of quartz and feldspar with two directions of fluidality. The microstructure is vitro-clastic and fluidal (Fig. 4A).

Volcanic glass The volcanic glass is grayish in color and composed essentially of spherolite with 0.1 to 3.5 mm size and associated with rare phenorcrysts (6 mm in size). The microstructure is spherolitic and fluidal.

Rhyolite The rhyolite is gray white to dark with phenocryst of sanidine and sometime quartz and oxides. Clinopyroxene is 0.2–2.5 cm in size and ranges from 2 to 30%. The matrix is made up of microlite of sanidine and oxides. The microstructure is porphyritic microlithic (Fig. 4B) and sometimes fluidal.

Breccia The phenocrysts in breccia consist of sanidine (5–10%), quartz (3–5%) sometimes bi-pyramidal, rock fragments essentially of rhyolite (25–30%), and some rare spherolites (< 1%). The size of the phenocrysts ranges from 0.5 to 9 mm. The matrix (55–60%) is the microlite of sanidine, which is associated with quartz and oxides. The microstructure is bracciated and fluidal (Fig. 4C).

Basalt/andesite These lithofacies are the more abundant between the studied pebble types. The degree of weathering makes them generally undifferentiated. The color is gray to dark gray. The phenocrysts are generally rare with sometimes automorphic plagioclase of 0.2 to 0.8 mm in size and less than 2%. The samples consist essentially of microlite of plagioclase associated with rare pyroxene, oxides, and glass. The microstructure is generally microlithic to aphyritic microlitic (Fig. 4D) and with sometimes the fluidality microstructure.

Fig. 4 Microphotographs. **A–D**
Microstructure photographs of
main representative pebbles:
A vitro-clastic and fluidal
microstructure (PL, ignim-
brite); **B** porphyritic microlitic
microstructure (PL, rhyolite); **C**
brecciated microstructure (PL,
volcanic breccia); **D** aphy-
ric microlitic microstructure
(PL, andesite). **E** to **F** Some
microstructure photographs of
volcanic rocks: **E** porphyritic
microlitic microstructure (PL,
olivine basalt); **F** spherulitic
microstructure (PL, cinerite).
G–P Representative heavy
minerals: **G** rutile (PPL); **H**
tourmaline (PPL); **I** brown
garnet (PPL); **J** epidote (PL); **K**
apatite (PL); **L** clinopyroxene
(PL); **M** orthopyroxene (PPL);
N zircon (PPL); **O** kyanite
(PPL); **P** biotite (PPL). NB:
PL polarized light, PPL plane
polarized light
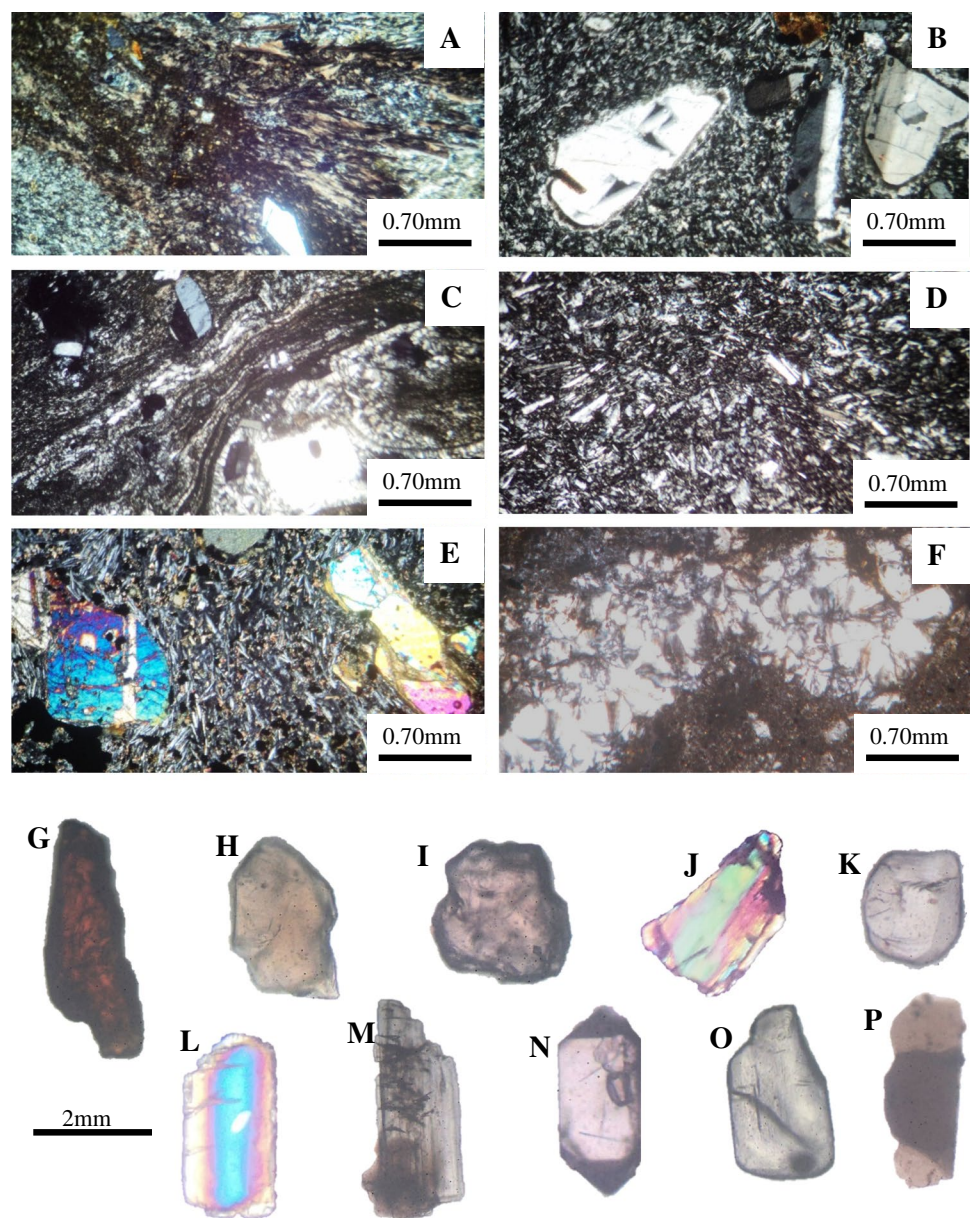
Trachyte The trachyte is more or less rare and weathered. The color is greenish gray. The phenocrysts are rare and represented by scattered sanidine in the microlitic matrix of feldspar. The microstructure is microlithic to aphyitic and fluidal.

Petrographic analyses of volcanic rocks

The volcanic rocks in the study area are represented by olivine bearing-basalt (TGB), cinerite (TGC), rhyolite

(TGR), ignimbrite, and volcanic tuff. The ignimbrite is deeply weathered, and the volcanic tuff is unconsolidated.

Basalt Basalt is black with visible olivine minerals. Under the microscope, the phenocrysts are made up of olivine (10–12%) and clinopyroxene (3–5%) with 0.2–3 mm in size. Olivine is generally cracked, and clinopyroxene is some-times weakly cracked. The matrix includes an association of microlith of plagioclase and oxides with olivine and pyrox-ene. The microstructure is porphyritic microlithic and more or less fluidal (Fig. 4E).

Cinerite Cinerite shows a whitish gray color under the microscope; the phenocrysts (5–8%) are represented by oriented quartz. sanidine, spherulite, and very rare plagioclase, with 0.2–1 mm sanidine essentially. The microstructure is microlitic to porphyritic microlithic tendency and sometimes spherulitic (Fig. 4F).

Rhyolite Rhyolite is clear gray in color. The phenocrysts (20–30%) are represented by quartz sometimes showing bipyramidal and corroded shapes, sanidine micro-fragments to trachyte. The size ranges from 0.5 to 1 mm. The matrix consists of microlith of quartz. Biotite, oxides, and sanidine are associated with glass phase. The microstructure is porphyritic microlitic and fluidal.

Heavy mineral analyses

Heavy mineral analyses have been carried out on the coarse-grained sediments including pebbly sands, pebbly silts, and sandy clay. The opaque minerals are the more abundant (75–93%) constituents, followed by zircon (3–13%) and garnet (1–5%). Other minerals such as tourmaline, apatite. Biotite, rutile, epidote, and pyroxene are generally less than 2%. Aluminum silicates are very rare, and the olivine is absent. The main specimens have been shown in Fig. 4G to P.

X-ray analyses

X-ray diffraction patterns of clayey samples (Fig. 5) indicate the presence of three common clay minerals including kaolinite, chlorite/smectite, and illite/muscovite with varied concentrations from the bottom to the top. The bottom sample (TGAG) is poor in clay minerals with only a minor quantity of kaolinite. The following samples (TGA1) is dominated by chlorite/smectite and associated with kaolinite. This chlorite/smectite fluctuated (decreases and increases from bottom to the top). Kaolinite appears at the bottom, increases progressively in samples TGA1 and TGA2I, and decreases progressively in sample TGC, TGA2S, and TGA3. The kaolinite increases again in sample TGA4 and finally disappears progressively towards the top. Illite/muscovite appears generally in a few quantities in some samples. Meanwhile, the important remark is the absence of illite/muscovite in the TGC sample and its presence in the TGA2I and TGA2S samples, between which it is interbedded. The non-clay minerals found in the studied samples include quartz (generally dominant), feldspar (plagioclase and sanidine mainly) and iron oxides (hematite, magnetite, and probably goethite) sometimes dominant (magnetite: TGA5 and TGA4-5). The quartz is more abundant than feldspar at the bottom but less abundant at the top (TGA6 and TGA7).

Geochemical analyses

Major elements

Major elements of the studied samples are reported in Table 2 and show that SiO_2 (42.84–68.65 wt%) and Al_2O_3 (15.39–27.95 wt%) are respectively the most abundant major elements, whereas CaO (0.11–0.95 wt%), MgO (0.09–0.92 wt%), P_2O_5 (0.04–0.32 wt%), MnO (< 0.01--0.92 wt%), and Cr_2O_3 (0.002–0.008 wt%) are respectively the less abundant with concentration < 1%. Fe_2O_3 (0.76–13.9 wt%), TiO_2 (0.88–2.29 wt%), K_2O (0.15–3.04 wt%), and Na_2O (0.03–2.67 wt%) are moderately represented.

The Na_2O/K_2O ratios vary from 0.20 to 0.99 indicating low proportion of plagioclase with respect of K-feldspar as display the petrographic analyses.

Major element enrichment factor diagram (Fig. 6A) normalized to PAAS displays a more or less strong depletion in P_2O_5, K_2O, CaO, and MgO for all the sample groups (mafic, intermediate, felsic, and recycled) with more depletion in the recycled samples, which is generally depleted except in SiO_2 and TiO_2 that are more enriched in this group. All the sample groups show a weak accumulation in TiO_2. The mafic sample group shows high enrichment in MnO and is more depleted in SiO_2.
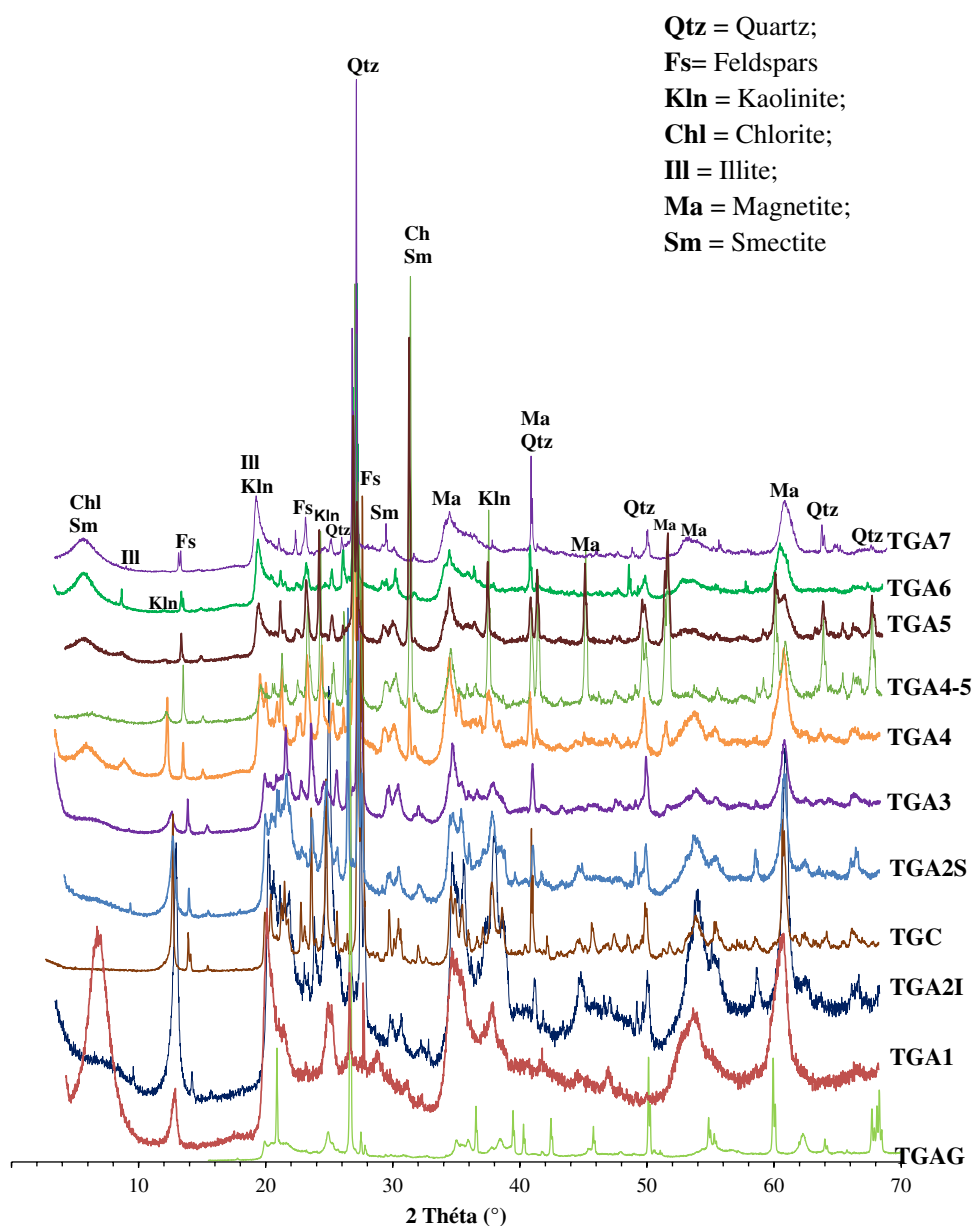
Trace elements

Trace elements of the studied samples have been tabulated in Table 3 and indicate that Zr (872.2–5584.7 ppm), Ba (53–1452 ppm), Nb (64.4–915.6 ppm), and Y (64.3–1352.1 ppm) are respectively the most abundant trace elements.

All the four sample groups cited in Table 3 show the same behavior of accumulation or depletion (Fig. 6B). All the sample groups display more or less accumulation in Y, Zr, U, Th, Ta, Nb, Hf, and Ga and depletion in V, Sr, Rb, Cs, Co, Sc, Ni, Cr, and Ba. Meanwhile mafic, intermediate, and felsic rocks show a strong accumulation in Ga, whereas the recycled group is neutral in this element.

Rare earth elements

The rare earth element (REE) concentration of the studied materials has been recorded in Table 3. The total REE content varies from 621.57 to 11,280.51 ppm. The HREE content (31.82 to 602.04 ppm) are low compared to LREE (what is the meaning of this item) (622.91 to 10,678.47 ppm). The LREE/HREE ratio ranges from 14.98 to 21.44 indicating enrichment in the LREE. REE patterns (Fig. 7A) normalized to PAAS (McLennan. 2001) are more or less flat with little accumulation in LREE and with significant negative Ce anomaly. The TGA1 sample is

Fig. 5 X-ray diffractions of representative studied samples

Qtz = Quartz;
Fs= Feldspars
Kln = Kaolinite;
Chl = Chlorite;
Ill = Illite;
Ma = Magnetite;
Sm = Smectite

more enriched compare to others. REE patterns of studied samples (Fig. 7) normalized to chrondrite (McDonough and Sun. 1995) are quite similar and show LREE enrichment with reference to HREE, negative Eu anomaly, and significant negative Ce anomaly. Negative Eu anomaly and LREE/HREE values ranging from 14.98 to 21.44 indicate moderate fractionation of REE.

Bau et al. (1996) have proposed the Ce/Ce* versus Pr/Pr* diagram (Fig. 7C) to discriminate the "real" from "false" Ce anomaly in the rock due to possible anomalous abundance of La. In this diagram, all the studied samples fall in field IIIb (negative Ce anomaly) except for only one sample that is located in field I (neither Ce nor La anomaly).

Discussion

Provenance

Several methods have been proposed for the sediment provenance such as microtexture and morphology of detrital zircon grains (e.g., Armstrong-Altrin 2020; Armstrong-Altrin et al. 2020), the trace element concentrations and/or their ratio values (e.g., the Cr and Ni concentrations; Garver et al. 1996), the major element concentrations and/or their ratio values (e.g., the SiO_2 content; Le Bas et al. 1986; the Al_2O_3/TiO_2 ratio; Hayashi et al. 1997), the REE patterns and the Eu anomaly (e.g., Cullers 2000), or the ratios between trace and major elements (e.g., TiO_2/Zr ratio; Girty et al. 1996). In

Table 2 Major element composition (wt%) and elemental ratios of the studied samples

	DL	SAMPLES												
		TGA1	TGA2I	TGC	TGA2S	TGS1	TGA3	TGA4	TGA4-5	TGA5	TGA6	TGA7	TGAG	TGSAS
SiO_2	0.01	42.84	45.57	54.08	51.11	56.09	58.06	52.25	43.86	51.64	55.97	54.15	68.65	74.47
Al_2O_3	0.01	20.78	25.68	27.95	21.06	19.31	19.46	21.15	13.22	15.39	15.83	17.31	17.55	14.43
Fe_2O_3	0.04	7.13	3.36	0.76	2.6	2.56	2.94	4.27	19.94	13.9	5.62	6.83	1.52	0.97
MgO	0.01	0.46	0.33	0.09	0.19	0.19	0.36	0.4	0.31	0.64	0.92	0.92	0.18	0.14
CaO	0.01	0.28	0.31	0.79	0.22	0.24	0.47	0.67	0.5	0.76	0.95	0.91	0.11	0.1
Na_2O	0.01	0.03	0.55	2.67	0.89	1.42	2.27	1.66	2.32	2.06	1.38	1.39	0.19	0.3
K_2O	0.01	0.15	1.02	3.04	1.45	2.3	2.47	1.68	2.37	2.17	2.06	1.62	0.92	1.09
TiO_2	0.01	2.29	1.28	1.06	1.29	1.3	1.06	1.5	0.77	0.93	0.88	1.01	1.54	1.16
P_2O_5	0.01	0.32	0.14	0.18	0.11	0.12	0.07	0.13	0.04	0.07	0.04	0.06	0.08	0.05
MnO	0.01	<0.01	0.03	<0.01	0.02	0.02	0.02	0.1	1.97	0.92	0.05	0.07	0.01	0.18
Cr_2O_3	0.002	0.007	0.008	0.004	0.006	0.005	0.004	0.003	0.002	0.002	0.003	0.002	0.01	0.008
LOI	-5.1	23.2	21.1	8.6	20.5	15.9	12.4	15.5	14.3	11	15.9	15.2	8.7	6.7
Sum	0.01	97.54	99.47	99.41	99.5	99.55	99.64	99.3	99.69	99.53	99.65	99.52	99.47	99.62
SiO_2/Al_2O_3	-	2.06	1.77	1.93	2.43	2.90	2.98	2.47	3.32	3.36	3.54	3.13	3.91	5.16
Na_2O/K_2O	-	0.20	0.54	0.88	0.61	0.62	0.92	0.99	0.98	0.95	0.67	0.86	0.21	0.28
K_2O/Al_2O_3	-	0.01	0.04	0.11	0.07	0.12	0.13	0.08	0.18	0.14	0.13	0.09	0.05	0.08
Al_2O_3/TiO_2	-	9.07	20.06	26.37	16.33	14.85	18.36	14.10	17.17	16.55	17.99	17.14	11.40	12.44
Fe_2O_3/K_2O	-	47.53	3.29	0.25	1.79	1.11	1.19	2.54	8.41	6.41	2.73	4.22	1.65	0.89
CIA	-	99.00	93.18	81.13	89.16	82.98	78.88	84.06	71.81	75.52	78.29	81.54	93.50	90.64
PIA	-	99.71	96.63	87.80	94.64	91.11	86.11	89.31	79.37	82.42	85.53	87.22	98.23	97.09
ICV	-	0.50	0.27	0.30	0.32	0.41	0.49	0.48	1.98	1.33	0.75	0.73	0.25	0.26
CIW	-	99.71	96.76	88.98	94.99	92.08	87.66	90.08	82.42	84.51	87.17	88.27	98.32	97.30

CIA (%) = [$Al_2O_3/(Al_2O_3 + CaO* + Na_2O + K_2O)$] × 100 from Nesbitt and Young (1982), PIA (%) = [$Al_2O_3 — K_2O /(Al_2O_3 + CaO* + Na_2O − K_2O)$] × 100 from Nesbitt and Young (1982) and Fedo et al. (1995); IVC = ($FeO_3 + K_2O + Na_2O + CaO + MgO + TiO_2)/Al_2O_3$ from Cox et al. (1995); CIW = [$Al_2O_3/(Al_2O_3 + CaO* + Na_2O)$] × 100 from Harnois (1988)

LOI loss of ignition

this study, we use the Roser and Korsch (1988) discriminant plot, widely and successfully used (e.g., Armstrong-Altrin et al. 2015; Zaid 2015; Tawfik et al. 2017). This diagram discriminates four major provenance types: recycled mature quartzose, felsic, intermediate, and mafic provenance sectors. Our studied samples occupy all the provenance fields with dominance of mafic to intermediate igneous provenance (Fig. 8A).

The Al_2O_3/TiO_2 ratio has been also widely used to constrain the provenance (e.g., Absar and Sreenivas 2015; Armstrong-Altrin et al. 2015, 2021; Zhou et al. 2015; Tawfik et al. 2017; Al-Juboury et al. 2021; Tchouatcha et al. 2021a), as they are immobile during sedimentary process (Taylor and McLennan 1985; Absar and Sreenivas 2015). This ratio varies from 3 to 8. 8 to 21 and 21 to 70, respectively for mafic, intermediate, and felsic igneous rocks (Hayashi et al. 1997). In our studied materials, this ratio varies from 9.70 to 26.37, which indicates heterogeneous sources. The SiO_2 content in sediment is also used to infer the rock composition (Le Bas et al. 1986) and has been used as well as for ancient sediments (Hayashi

et al. 1997) and recent deposits (Armstrong-Altrin 2009; Armstrong-Altrin et al. 2021). According to the Al_2O_3/TiO_2 vs. SiO_2 plot (Fig. 8B), the samples from the Ngwa Basin indicate the heterogeneous source with dominant intermediate composition.

Cr and Ni trace elements are indicator of source rock composition (Garver et al. 1996), and high concentrations of these trace elements are related to mafic rocks and/or minerals (e.g., Armstrong-Altrin et al. 2019; Ndjigui et al. 2019; Tchouatcha et al. 2021a); in the studied sediments, the PAAS normalized values of trace elements of studied samples (Fig. 6B) are depleted in Cr and Ni indicating the important contribution of felsic rocks.

Moreover, the Eu anomaly and chondrite normalized REE patterns are also applied to predict the composition of source rock of sediments (e.g., Cullers 2000; Kettanah et al. 2021; Madhavaraju et al. 2021; Ramos-Vazquez and Armstrong-Altrin 2019; 2021). The REE pattern normalized to chondrites of studied sediments (Fig. 7B) show a little significant positive and some no Eu anomalies, showing also a heterogeneous source.
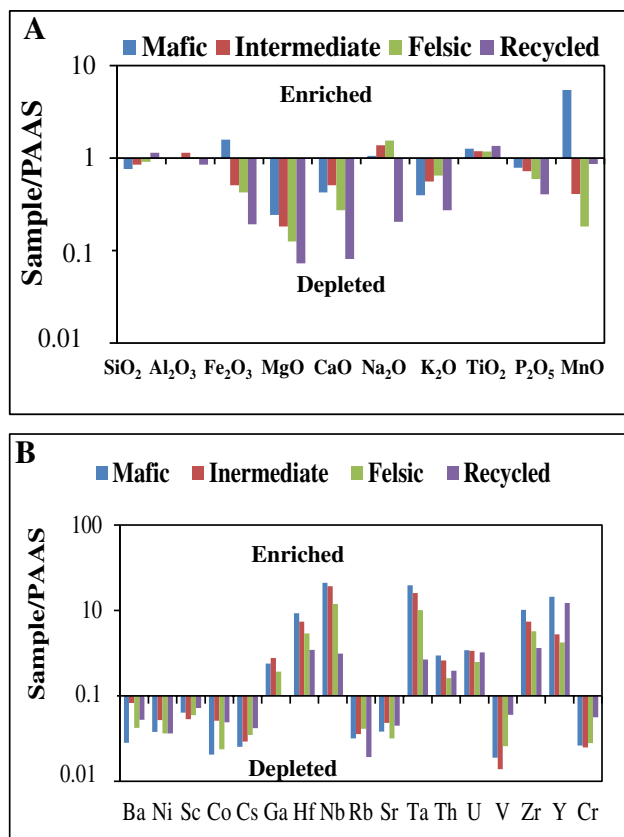
Fig. 6 Major and trace elements correlation diagrams: **A** stick diagram of average major elements for the studied sediments; **B** stick diagram of average trace elements for the studied sediments, data are average values normalized to PAAS (after Taylor and McLennan 1985)

The heavy minerals have been also used as indicators of sediment provenance (e.g., Acquafredda et al. 1997; Tchouatcha et al. 2010, 2021b; Mendes et al. 2020). In our sediments, the rarity of aluminum silicates indicates the weak contribution of metamorphic rocks. The minerals such as pyroxenes, although their low concentrations (< 2%), would indicate volcanic source, and they are frequents in the recent sediments of volcanic areas: in the Djerem-Mbere Basin, Cameroon (Tchouatcha et al. 2010), and the southern Apennines, Italy (Acquafredda et al. 1997). Tourmaline and biotite are also very low and reported in the lower part of deposits, associated with rare kyanite and more or less abundant muscovite suggesting likely the metamorphic and plutonic contributions. So, the distributive sources of sediments vary from bottom to top of the stratigraphic sequence, as indicate the geochemical data: felsic source at bottom (TGAG and TGSAS) and intermediate to mafic sources in the middle and the upper part of deposits.

According to Herron's classification diagram (Herron 1988) (Fig. 8C), the studied samples correspond essentially to shale (TGA2I, TGA2S, TGC, TGA3, TGA4, TGA6,

TGAG, and TGS1), Fe-shale (TGA1, TGA5, TGA4-5, and TGA7), and Wacke (TGSAS).

To determine the source rock composition and evaluate the rate of weathering, and eventually the K-enrichment, the samples were plotted in the $Al_2O_3 - (Ca*O + Na_2O) - K_2O$ (Fig. 9A) and $Al_2O_3 - (Ca*O + Na_2O + K_2O) - FeO + MgO$ (Fig. 9B) diagrams (Nesbitt and Young 1984, 1989, modified). In these diagrams, the source rock composition which have been experienced moderate to high degree of chemical weathering are varied, dominated by rhyodacite composition, and associated with andesitic and basaltic composition. The rhyodacite is the intermediate rock between rhyolite and dacite, and this last is associated either to andesite or to rhyolite in the ignimbrite. Moreover, the petrographic data of pebbles from the deposits and their concentration indicate the abundant andesite/basalt associated with rhyolite, trachyte, breccias, and ignimbrite, and this composition indicates the heterogeneous source rocks as the geochemical data. Figure 9A also shows varied values of chemical indices and clay mineral contents, probably linked to variation of the source rock composition and climatic conditions. More, the samples plot perpendicularly to the CN–K apex indicate the presence and more or less equal proportions of Ca- and/ or Na-bearing minerals (plagioclase) and K-bearing minerals (sanidine) in the source rocks, as confirmed the petrographic data. The Na_2O and CaO are leached out from the earlier dissolved plagioclase and K_2O from sanidine, and the increasing degree of weathering leads to the loss of Ca^{2+}, Na^+, and K^+.

Sediment sorting, recycling, and paleo-weathering

Chemical index of alteration (CIA) of Nesbitt and Young (1982), plagioclase index of alteration (PIA; Nesbitt and Young 1982; Fedo et al. 1995), and index of compositional variability (ICV) of Cox et al. (1995) have been successfully used to indicate compositional maturity and/or chemical weathering of sediments (e.g., Mongelli et al. 2006; Perri et al. 2011. Perri 2014; Tawfik et al. 2017 for CIA; Armstrong-Altrin et al. 2015; Rashid et al. 2015 for CIA and PIA; Ngueutchoua et al. 2019; Tchouatcha et al. 2021a for CIA, PIA and ICV). PIA and CIA values > 75 and ≤ 50 indicate respectively intense and low chemical weathering of source rocks, and IVC values > 1 and < 1 indicate respectively immature and mature character of sediments. CIA and PIA values of studied sediments range respectively from 71.81 to 99.00 and 79.37 to 99.71, which indicate intense chemical weathering of rock sources. ICV values vary between 0.25 and 1.9, but generally < 1 indicating the maturity of our studied sediments.

Furthermore, according to Zou et al. (2016), high $\sum$REE contents indicate a possible control by differing

Table 3 Trace and rare earth element composition (ppm) and elemental ratios of the studied samples

	DL	SAMPLES												
		TGA1	TGA2I	TGC	TGA2S	TGS1	TGA3	TGA4	TGA4-5	TGA5	TGA6	TGA7	TGAG	TGSAS
Ba	1	53	278	1452	235	313	234	103	328	110	354	147	280	403
Ni	20	20	24	54	20	20	20	20	20	20	20	20	20	20
Sc	1	16	15	8	11	10	9	10	6	7	5	7	13	10
Be	1	3	13	8	10	5	10	9	2	9	6	9	3	3
Co	0.2	1	15.2	29.9	12.3	8.8	2.1	0.9	2.2	0.7	3.8	4.4	5.1	17.5
Cs	0.1	0.4	3	0.1	1.5	1.9	1.7	1.2	1.5	1.3	3.2	0.3	2.5	1.8
Ga	0.5	81.6	45.2	80.4	40.7	34.6	42.1	63.8	27.9	42.9	36.3	40.6	22	17.3
Hf	0.1	119.9	29.7	37.4	28.6	23.8	29.8	57.8	18.8	34.4	23.4	29.3	19.7	14.8
Nb	0.1	915.6	235.9	452.2	235.3	181.3	269.8	543.8	203.6	346.2	224.1	291.2	64.4	54.1
Rb	0.1	9.6	46.9	27.4	45.7	64.6	66.7	57.7	66.9	96.1	96.4	33.3	31.2	30.3
Sn	1	30	8	12	7	6	8	14	4	8	6	8	3	2
Sr	0.5	40.9	79.4	105.8	60.4	61	65.3	85.3	63.8	95.7	133.2	102.1	91.2	87.6
Ta	0.1	67.6	13.8	21.8	13.3	10.5	15.3	33.1	9.6	19.2	13.4	16	3.9	2.9
Th	0.2	115.9	31.3	50.7	29.8	22	25.1	51.1	15.3	28.5	20	24.9	27.7	29.8
U	0.1	23.2	9.5	10.9	11.7	8.8	6.6	13.4	4.7	8	5.6	7.4	10.9	9.1
V	8	46	59	8	44	48	29	18	8	10	13	19	99	80
W	0.5	5.8	3.1	3.9	2.6	2.5	2.6	7	2.4	3	3.3	3.4	1.9	1.8
Zr	0.1	5584.7	1269	1346.7	1250.6	1075.3	1317.5	2532.4	944.30	1530	1060.8	1344.40	872.2	651.7
Y	0.1	1352.1	298	142.6	197.5	151.1	76.3	162.5	76.30	97.1	64.3	118.20	384.4	273.1
Cr		47.894	54.736	27.368	41.052	34.21	27.368	20.526	13.684	13.684	20.526	13.684	68.42	54.736
La	0.1	4146.8	492.3	374	400.5	332.9	167.9	368.8	148.20	268.5	171.7	343.60	899.5	664.5
Ce	0.1	1916.5	567.5	743.2	493.6	399.8	266.4	698.8	276.90	502.6	305.6	602.10	257.9	246.6
Pr	0.02	845.21	73.44	88.9	93.46	75.66	33.94	78.82	28.69	56.28	36.8	80.13	187.97	140.74
Nd	0.3	2924.3	265.8	321.3	331.8	260.8	116.6	265.7	99.20	187.8	125.2	267.4	645.8	487.9
Sm	0.05	435.37	42.41	54.49	56.03	43.3	19.07	43.48	16.15	30.23	20.26	41.13	96.91	71.9
Eu	0.02	79.42	7.7	12.05	9.72	7.83	3.66	8.77	3.14	5.76	3.79	8.07	14.48	10.46
Gd	0.05	330.87	46.35	40.43	44.52	34.68	15.34	34.69	14.09	23.74	14.98	30.62	76.36	57.44
Tb	0.01	48.89	6.81	6.04	6.85	5.4	2.43	5.46	2.18	3.78	2.36	4.81	10.9	8.03
Dy	0.05	257.31	39.4	31.76	37.56	29.45	14.09	31.26	12.54	21.17	12.91	25.83	56.6	40.5
Ho	0.02	47.67	8.45	5.82	7.14	5.56	2.79	6.15	2.57	3.93	2.43	4.78	10.77	7.75
Er	0.03	125.23	23.01	15.61	19.77	14.98	7.92	17.02	7.8	10.97	6.42	12.85	29.01	20.39
Tm	0.01	16.03	2.95	2.11	2.71	2.11	1.22	2.41	1.16	1.54	0.94	1.81	3.7	2.59
Yb	0.05	93.36	16.69	13.09	16.63	13.02	7.59	14.97	7.73	10.14	5.98	11.09	20.55	14.67
Lu	0.01	13.55	2.51	1.81	2.47	1.89	1.18	2.17	1.22	1.47	0.85	1.6	3.2	2.29
LREE/HREE	-	17.74	14.98	21.44	15.35	15.95	16.74	18.87	16.66	20.28	21.27	21.87	16.17	17.46
Eu/Eu*	-	0.99	0.74	1.21	0.92	0.95	1.01	1.06	0.98	1.01	1.02	1.07	0.79	0.77
Ce/Ce*	-	0.24	0.69	0.94	0.59	0.58	0.81	0.95	0.98	0.94	0.89	0.84	0.14	0.19
Pr/Pr*	-	2.10	1.11	1.07	1.36	1.38	1.13	1.08	1.02	1.08	1.11	1.17	2.71	2.39

$Eu/Eu* = (Eu_{sample}/Eu_{PAAS})/(Sm_{sample}/Sm_{PAAS})^{1/2}(Gd_{sample}/Gd_{PAAS})^{1/2}$;　$Ce/Ce* = (Ce_{sample}/Ce_{PAAS})/(La_{sample}/La_{PAAS})^{1/2}(Pr_{sample}/Pr_{PAAS})^{.1/2}$;　$Pr/Pr* = (0.5Ce + 0.5Nd)$

amount of accessory minerals such as zircon linked to recycling processes. The $\sum$REE for the studied sediments ranges from 621.57 to 11,280.5 ppm, which are notably higher than the PAAS (184.77 ppm), and this indicates high recycling of the studied sediments.

Paleo-climate and paleo-oxidation condition

Many parameters such as CIA has been widely applied for paleo-climate interpretation from formations of varied age (e.g., Nesbitt and Young 1984; Yan et al. 2010; Zeng et al. 2019; Tchouatcha et al. 2021a). Low values (˂60) and high
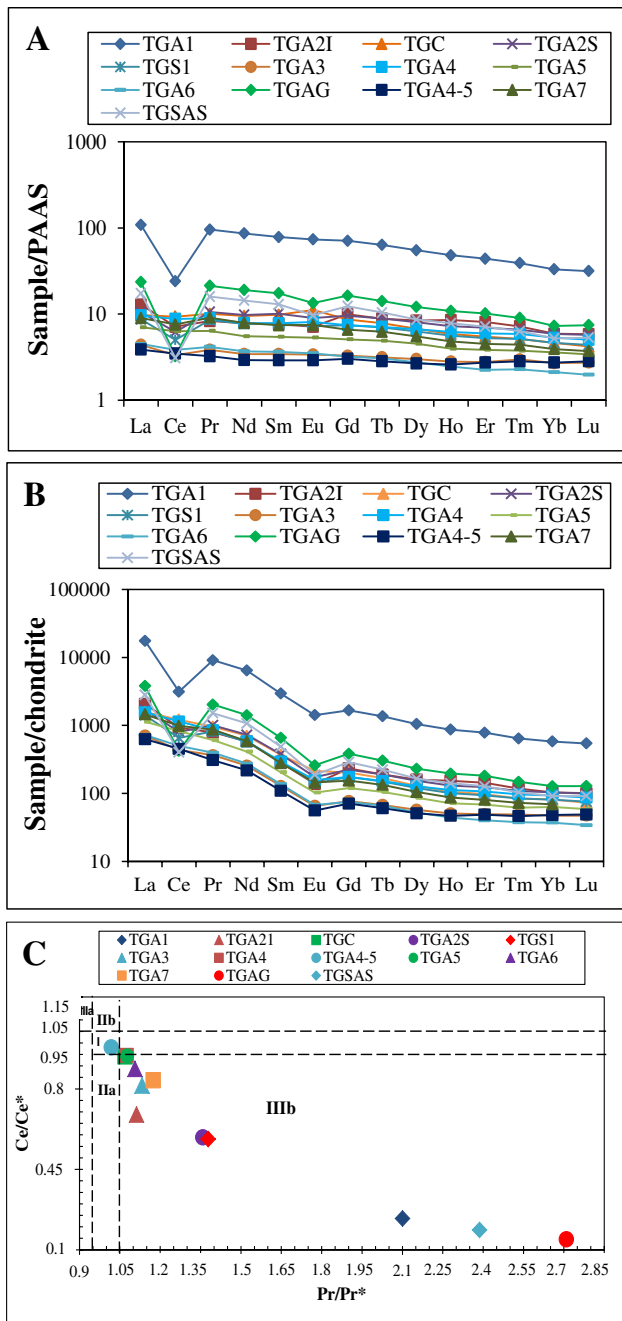
Fig. 7 Rare earth element correlation diagrams: **A** PAAS-normalized REE patterns; **B** chondrite-normalized REE patterns (after McLennan 2001 and McDonough and Sun 1995, respectively); **C** PAAS normalized cross plot diagram of Ce/Ce* vs. Pr/Pr* used as a proxy for the Ce and La anomalies (modified after Bau et al. 1996). Field I: neither Ce nor La anomaly; Field IIa: positive La anomaly, no Ce anomaly; Field IIb: negative La anomaly, no Ce anomaly; Field IIIa: positive Ce anomaly, negative La anomaly; Field IIIb: negative Ce anomaly

Fig. 8 Provenance and classification diagrams: **A** provenance discriminant function plot (after Roser and Korsch 1988); **B** SiO$_2$ vs. Al$_2$O$_3$/Ti$_2$O bivariate plot; **C** classification according to the scheme of Herron (1988) for the Ngwa studied samples

values (> 80) of CIA indicates, respectively, cold and dry climate during low chemical weathering and warm and humid climate during high chemical weathering (White and Blum 1995). For our samples, CIA values range from 71.81

to 97.83, which indicate moderate to high chemical weathering under warm and semi humid conditions.
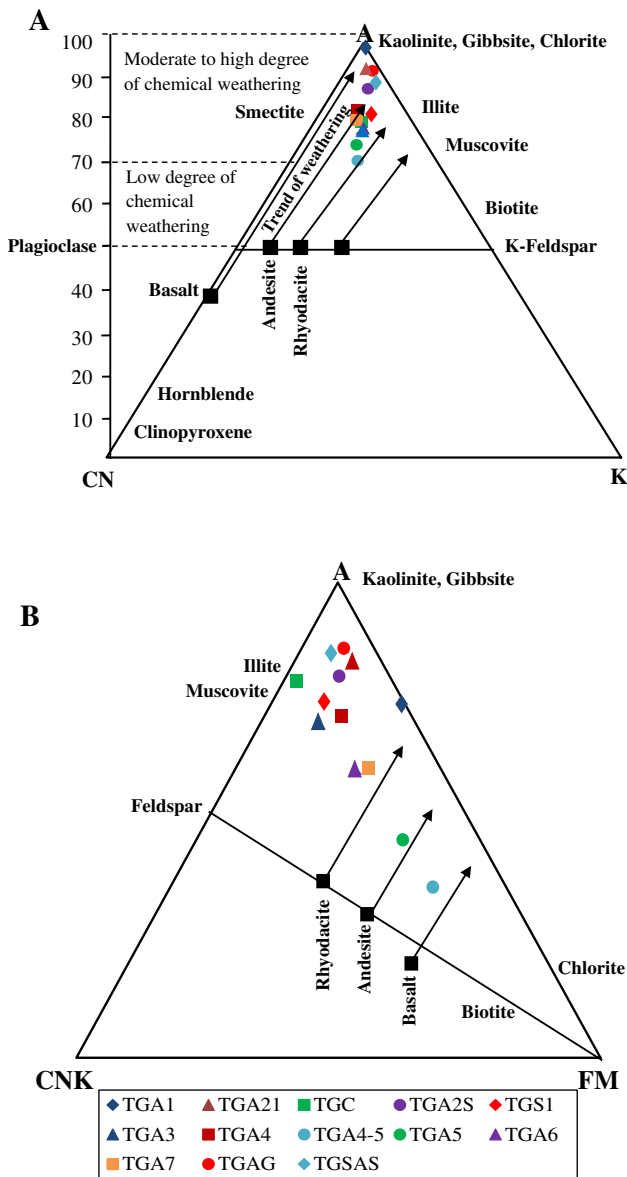
Fig. 9 Ternary diagrams: **A** A-CN-K plot; **B** A-CNK-FM plot, A = Al_2O_3, C = CaO*, N = Na_2O, K = K_2O, F = total Fe as FeO, and M = MgO (modified after Nesbitt and Young 1984, 1989)

Furthermore, the clay minerals respond to their chemical and thermal environment of deposition. The transport and sedimentation of the clay minerals follow mutation from their origin in the clay cycle (Velde 1992). Illite and chlorite form the base of digenetic zone (Dunoyer De Segonzac 1970). Kaolinite is abundant in hot and humid environment, and their presence indicates intense weathering of source rocks with steep relief and exhaustive leaching of weathered materials (Enu 1986). According to the X-ray diffraction data and concentration variations of kaolinite, the climate was more or less hot and arid to semi-arid but with more arid conditions developed towards the top of the sequence.

Generally, the variation in kaolinite concentration is related to that of Sm/Chl which would indicate a less humid to semi-humide climate, muscovite characterized terrestrial source. The absence of illite/muscovite in the TGC sample and its presence in the TGA2S and TGA2I between which it is interbedded indicate their terrestrial source and would correspond to muscovite.

Depositional environment

Conglomeratic facies

- The Gcm lithofacies is a result of high-power debris and gravity flows on a steep topographic gradient (Nilsen 1982). The predominant clast-supported nature indicates that the flows were highly concentrated and that the clasts remained closely packed during deposition.
- The Gmi lithofacies is attributed to stream flow processes resulting from a bed load traction carpet (Nilsen 1982) of high-energy gravity deposits on a steep topographic gradient (Nemec and Steel. 1984; Miall 1996).
- The Gmm lithofacies is interpreted as cohesion less debris flow (Nilsen 1982).

Sandstone facies

- The Sm lithofacies is interpreted as sands deposited rapidly from turbulent suspension by hyper-concentrated mass flows or subaqueous high-density turbidity currents (Ghibaudo 1992).
- The Sh lithofacies is attributed to planar bed flows of shallow high velocity (Miall 1978; Harms et al. 1995).

Claystones/siltstone facies

- The Fm lithofacies result from more or less rapid deposition from suspension and from weak traction current (Miall 1996).
- The Fh lithofacies is common in the overbank area, and represents deposition from suspension and/or by weak traction current (Miall 1996).
- The Fhfc lithofacies indicates the abundance of leaf fossils and coals in the clay facies (Fh) indicating the abundance of vegetation.

Furthermore, rock samples analyzed by X-Ray diffractions have been selected from the base to the top of the stratigraphic sequence. In spite of samples TGAG and TGA1 have been collected from two sites at the same stratigraphic position; their difference in mineralogical and chemical compositions is probably related to the mechanism of sediment distribution in the basin influenced by lithology of source

Fig. 10 Discriminant diagrams to understand the different tectonic settings of the studied sediments from the Ngwa Basin: **A** discriminant-function multi-dimensional diagram for high-silica clastic sediments (after Verma and Armstrong-Altrin 2013). The subscript m_1 in DF1 and DF2 represents the high silica diagram based on log_e-ratios of major-elements. The discriminant function equations are **DF1(Arc-Rift-Col)m$_1$** $= (-0.263 \times \ln(TiO_2/SiO_2))_{adj} + (0.604 \times \ln(Al_2O_3/SiO_2))_{adj} + (-1.725 \times \ln(Fe_2O_{3t}/SiO_2))_{adj} + (0.660 \times \ln(MnO/SiO_2))_{adj} + (2.191 \times \ln(MgO/SiO_2))_{adj} + (0.144 \times \ln(CaO/SiO_2))_{adj} + (-1.304 \times \ln(Na_2O/SiO_2))_{adj} + (0.054 \times \ln(K_2O/SiO_2))_{adj} + (-0.330 \times \ln(P_2O_5/SiO_2))_{adj} + 1.588$; **DF2(Arc-Rift-Col)m$_1$** $= (-1.196 \times \ln(TiO_2/SiO_2))_{adj} + (1.604 \times \ln(Al_2O_3/SiO_2))_{adj} + (0.303 \times \ln(Fe_2O_{3t}/SiO_2))_{adj} + (0.436 \times \ln(MnO/SiO_2))_{adj} + (0.838 \times \ln(MgO/SiO_2))_{adj} + (-0.407 \times \ln(CaO/SiO_2))_{adj} + (1.021 \times \ln(Na_2O/SiO_2))_{adj} + (-1.706 \times \ln(K_2O/SiO_2))_{adj} + (-0.126 \times \ln(P_2O_5/SiO_2))_{adj} - 1.068$; (B) discriminant-function multi-dimensional diagram for low-silica clastic sediments (Verma and Armstrong-Altrin 2013). The subscript m_2 in DF1 and DF2 represents the low silica diagram based on log_e-ratios of major-elements. The discriminant function equations are **DF1(Arc-Rift-Col)m2** $= (0.608 \times \ln(TiO_2/SiO_2)_{adj}) + (-1.854 \times \ln(Al_2O_3/SiO_2)_{adj}) + (0.299 \times \ln(Fe_2O_3^t/SiO_2)_{adj}) + (-0.550 \times \ln(MnO/SiO_2)_{adj}) + (0.120 \times \ln(MgO/SiO_2)_{adj}) + (0.194 \times \ln(CaO/SiO_2)_{adj}) + (-1.510 \times \ln(Na_2O/SiO_2)_{adj}) + (1.941 \times \ln(K_2O/SiO_2)_{adj}) + (0.003 \times \ln(P_2O_5/SiO_2)_{adj}) - 0.294$; **DF2(Arc-Rift-Col)m2** $= (-0.554 \times \ln(TiO_2/SiO_2)_{adj}) + (-0.995 \times \ln(Al_2O_3/SiO_2)_{adj}) + (1.765 \times \ln(Fe_2O_3.^t/SiO_2)_{adj}) + (-1.391 \times \ln(MnO/SiO_2)_{adj}) + (-1.034 \times \ln(MgO/SiO_2)_{adj}) + (0.225 \times \ln(CaO/SiO_2)_{adj}) + (0.713 \times \ln(Na_2O/SiO_2)_{adj}) + (0.330 \times \ln(K_2O/SiO_2)_{adj}) + (-0.637 \times \ln(P_2O_5/SiO_2)_{adj}) - 3.631$; **C** tectonic discrimination plot (after Roser and Korsch 1986)

rocks. This would explain several input sources in a fluvial network.

Tectonic setting

For this work, to shed some light on the tectonic setting of the study area, the discriminant-function-based major-element diagrams of Verma and Armstrong-Altrin (2013) have been applied. These diagrams have been widely used for recent and ancient deposits (e.g., Guadagnin et al. 2015; Nagarajan et al. 2015; Armstrong-Altrin and Machain-Castillo 2016; Tawfik et al. 2017; Zeng et al. 2019; Tchouatcha et al. 2021a). These diagrams differentiate between three fields of tectonic settings including continental arc, island continental rift and collision from high-silica ((SiO_2)adj = 63–95%), and low-silica ((SiO_2)adj = 35–63%). For the studied sediments, seven samples belong to high-silica and six samples belong to low-silica diagrams (Fig. 10A and B). The majority of studied samples fall in the rift field and at the border with collision field in the high silica multidimensional diagram and within the Arc field in the low silica multidimensional diagram. By using the tectonic discrimination plot (Fig. 10C) of Roser and Korsch (1986), most of the studied samples fall mainly in the active continental margin, but some samples fall in the passive continental
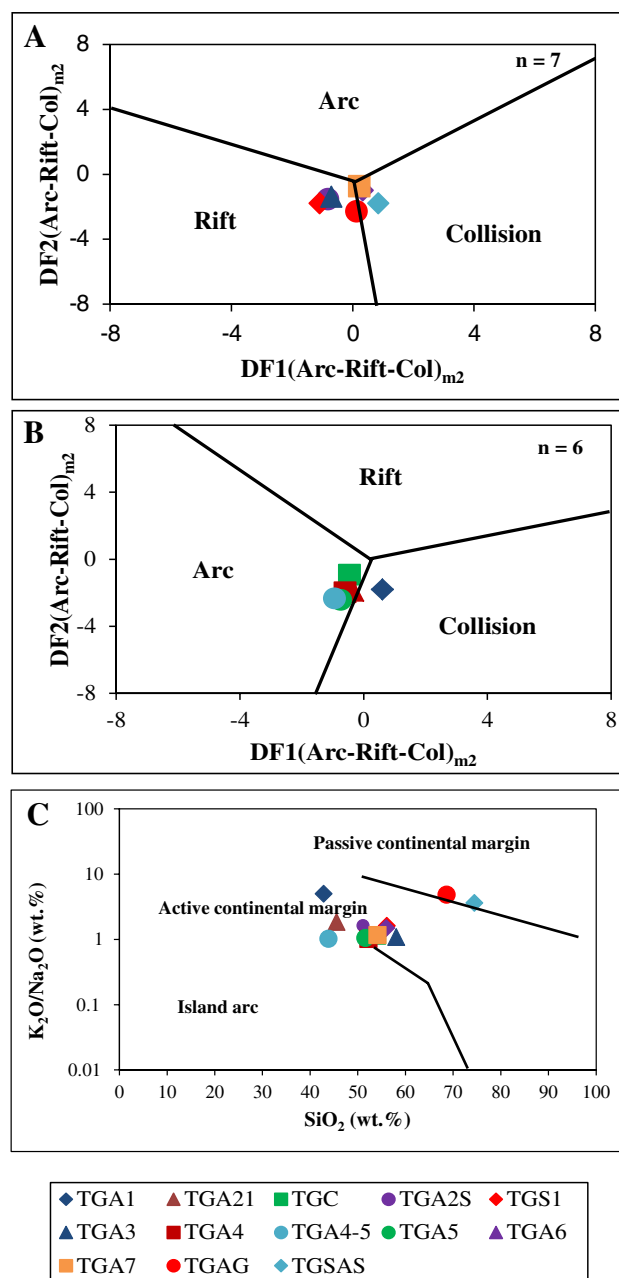
margin. This result could indicate a composite tectonic setting (transpressive to extensional tectonics), which led to the setting up of the Cameroon Volcanic Line. The Ngwa Basin is located along the Cameroon Volcanic Line. The CVL, the Volcano-tectonic megatructure enclosed in the pan-African field belt (Njonfang 1998), is a stress megasplit of 30° E trend generated by the pre-Cambrian leap reactivation N 70°E (Cornacchia and Dars 1983; Moreau et al. 1987; Deruelle et al. 1991; Montigny et al. 2004). This pre-Cambrian fault (CCSZ: Centre Cameroon Shear Zone) had been reactivated several times during the Phanerozoic

period (Ngangom 1983; Tchouatcha 2011). These phases of reactivation have led to the reconstruction of volcanic massifs and the setting up of the Ngwa Basin and probably connected to the Late Jurassic-Early Cretaceous Gondwanan continental rifting and the South Atlantic Ocean evolution during the Cenozoic period.

Conclusion

The fine-grained sediments of the Ngwa Basin consist mainly of shale with some rare wacke (TGSAS). These fine-grained sediments are mature sediments and underwent intense chemical weathering of rock sources. The source sediments are essentially volcanic and heterogeneous with dominance of mafic to intermediate igneous provenance. They made up essentially of andesite and basalt, associated with rhyolite, dacite, ignimbrite, and trachyte. The presence of only quartz pebbles in the basal deposit indicates recycled and probably metamorphic and granitic sources.

The variation of the geochemical composition signature (felsic, intermediate, and mafic composition) from the bottom to the top of the sequence is linked to the lithology of eroded source rocks influenced by the amount of pyroclastic input.

The studied samples probably have a composite setting ranging from transpressive to extensional tectonic. This composite tectonic setting led to the setting up of the Cameroon Volcanic Line along which is located the Ngwa Basin.

It is postulated that the climate of deposition was warm and arid to semi humid, but more arid at the end of deposition of the studied section. The sedimentation regime varied from high to low energy related to tectonic and climatic mechanisms. Inside the depositional basin, it is inferred that the deposition took place in the oxic water column with several input sources debouching into the basin. The evolution of conditions and environments of sedimentation are probably linked to tectonics and climate.

Declarations

References

Absar N, Sreenivas B (2015) Petrology and geochemistry of greywackes of the ~1.6 Ga Middle Aravalli supergroup, northwest India: evidence for active margin processes. Int Geol Rev 57:134–158

Acquafredda P, Fornelli A, Piccarreta G, Summa V (1997) Provenance and tectonic implications of heavy minerals in Pliocene-Pleistocene siliciclastic sediments of the southern Apennines. Italy Sediment Geol 113(1–2):149–159

Al-Juboury A, Hussain SH, Al-Lhaebi SH (2021) Geochemistry and mineralogy of the Silurian Akkas Formation, Iraqi western desert: implications for palaeoweathering, provenance and tectonic setting. Arab J Geosci 14:760

Armstrong-Altrin JS (2009) Provenance of sands from cazones, Acapulco, and Bahía Kino beaches. Mexico Rev Mex Ciencias Geol 26(3):764–782

Armstrong-Altrin JS (2020) Detrital zircon U-Pb geochronology and geochemistry of the Riachuelos and Palma Sola beach sediments, Veracruz State, Gulf of Mexico: a new insight on palaeoenvironment. J Palaeogeogr 9(4):28

Armstrong-Altrin JS, Machain-Castillo ML (2016) Mineralogy, geochemistry and radiocarbon ages of deep sea sediments from the Gulf of Mexico. Mexico J South Amer Earth Sci 71:182–200

Armstrong-Altrin JS, Nagarajan R, Balaram V, Natalhy-Pineda O (2015) Petrography and geochemistry of sand from the Chachalacas and Veracruz beach areas, western Gulf of Mexico. Mexico: constraints on provenance and tectonic setting. J South Amer Earth Sci 64:199–216

Armstrong-Altrin JS, Botello AV, Villanueva SF, Soto LA (2019) Geochemistry of surface sediments from the northwestern Gulf of Mexico: implications for provenance and heavy metal contamination. Geol Q 63(3):522–538

Armstrong-Altrin JS, Ramos-Vazquez MA, Hermenegildo-Ruiz NY, Madhavaraju J (2020) Microtexture and U-Pb geochronology of detrital zircon grains in the Chachalacas beach, Veracruz State. Gulf of Mexico Geol J 56(5):2418–2438

Armstrong-Altrin JS, Madhavaraju J, Vega-Bautista F, Ramos-Vazquez MA, Perez-Alvarado BY, Kasper-Zubillaga JJ, Ekoa Bessa AZ (2021) Mineralogy and geochemistry of Tecolutla and Coatzacoalcos beach sediments. SW Gulf of Mexico Applied Geol 134:105103

Bau M, Koschinsky A, Dulski P, Hein JR (1996) Comparison of the partitioning behaviours of yttrium, rare earth elements and titanium between hydrogenetic marine ferro-manganese crusts and seawater. Geochim Cosmochim Acta 60:1709–1725

Benammi M, Hell JV, Bessong M, Nolla D, Sole J, Brunet M (2017) Preliminary magnetostratigraphic and isotopic dating of the Ngwa Formation (Dschang. Western Cameroon). J Geol Geophys 6:282. https://doi.org/10.4172/2381-8719.1000282

Bessong M, Hell JV, Burkhardt Feist S, Samankassou E, Bennamid M, Nolla JD, Mbesse CO, Adatte T, Martini R, Brunet M (2017) First palynostratigraphical evidence for a Late Eocene to Early Miocene age of the volcano-sedimentary series of Dschang. western part of Cameroon and its implications for the interpretation of palaeoenvironment. Palaeogeogr Palaeoclimatol Palaeoecol 485:517–530

Bilobe JA, Feist-Burkhardt S, Eyong Takem J, Samankassou E (2021) Biostratigraphy of Cretaceous-Neogene sedimentary infill of the Mamfe basin, southwest Cameroon: paleoclimate implication. J Afr Earth Sci 182:104279

Capponi A (1945) La lignite de Dschang. Bull Soc Et Cam 7:75–86

Cornacchia M, Dars FI (1983) Un trait structural majeur du continent africain Les linéaments centrafricains du Cameroun au Golfe d'Aden. Bull Soc Géo France 7(1):101–109

Cox R, Lowe DR, Cullers RL (1995) The influence of sediment recycling and basement composition on evolution of mudrock chemistry in the southwestern United States. Geochem Cosmochim Acta 59:2919–2940

Cullers RL (2000) The geochemistry of shales, siltstones and sandstones of Pennsylvanian - Permian age, Colorado, U.S.A.:

Implications for provenance and metamorphic studies. Lithos 51:181–203

Deruelle B, Moreau C, Nkoumbou C, Kambou R, Lissom J, Njongfang E, Ghogomu RT, Nono A (1991) The Cameroon Line: a review. In: Kampunzu, A.B.. Lubala. R.T. (Eds.). Magmatism in extensional structural settings. The Phanerozoic of Africa Plate. Springer Berlin 274–327

Dunoyer De Segonzac G (1970) The transformation of clay minarals during diagenesis and lower-grade metamorphism: a review. Sedimentol 15:281–346

Enu E (1986) Influence of tectonic and palaeoenvironment on late Cretaceous clay sedimentation in the Upper Benue Trough. Nigeria Geol J 21:93–99

Eyong JT (2003) Litho-biostratigraphy of the Mamfe Basin. SW province of Cameroon. W. Africa. PhD Thesis. University of Leeds. United Kingdom

Fedo CM, Nesbitt HW, Young GM (1995) Unravelling the effects of Potassium metasomatism in sedimentary rocks and paleosols with implications for paleo-weathering conditions and provenance. Geol 23:921–924

Fosing EM, Mengou AC, Njanko T, Tefo FA, Tiseh IK, Chatue KM, Njiki C (2019) Emplacement of the Dschang granitic pluton (West-Cameroon): constraints from microstructures and magnetic fabrics. J Afr Earth Sci 156:144–157

Garver JI, Royce PR, Smick TA (1996) Chromium and nickel in shale of the Taconic Foreland: A case study for the provenance of fine-grained sediments with an ultramafic source. J Sediment Res 66:100–106

Ghibaudo G (1992) Subaqueous sediment gravity flow deposits: practical criteria for their description and classification. Sedimentol 39:423–454

Girty GH, Ridge DL, Knaack C, Johnson D, Al-Riyami RK (1996) Provenance and depositional setting of Paleozoic chert and argillite, Sierra Nevada, California. J Sediment Res 66:107–118

Guadagnin F, Junior FC, Magalhaes AJC, Alessandretti L, Ballico MB, Jelinek AR (2015) Sedimentary petrology and detrital zircon U-Pb and Lu–Hf constraints of Mesoproterozoic intracratonic sequences in the Espinhaço Supergroup: Implications for the Archean and Proterozoic evolution of the São Francisco Craton. Precamb Res 266:227–245

Guerrera F, Veneri F (1989) Edvidenze di attività vulcanica nei sedimenti neogenici e pleistocenici dell' Appennino: stato delle conoscenze. Boll Soc Geol Ita 108:121–160

Harms JC, Southard JB, Spearing DR, Walker RG (1995) Depositional environment interpreted from primary sedimentary and stratification sequences. SEPM. Short Course

Harnois L (1988) The CIW index: A new chemical index of weathering. Sediment Geol 55(3–4):319–322

Hayashi KI, Fujisawa H, Holland HD, Ohmoto H (1997) Geochemistry of ~1.9 Ga sedimentary rocks from northeastern Labrador Canada. Geochem Cosmochim Acta 16(19):4115–4137

Herron MM (1988) Geochemical classification of terrigenous sands and shales from core or log data. J Sediment Petrol 58:820–829

Kagou Dongmo A, Wandji P, Pouclet A, Vicat JP, Cheilletz A, Nkouathio DG, Alexandrov P, Tchoua F (2001) Evolution volcanologique du Mont Manengouba (Ligne du Cameroun), nouvelles données pétrographiques, géochimiques et géochronologiques. Compt Rend Acad Sci Paris Ser IIa 333:155–162

Kagou Dongmo A, Nkouathio D, Pouclet A, Bardintzeff JM, Wandji P, Nono A, Guillou H (2010) The discovery of Late Quaternary basalt on Mount Bambouto: implications for recent widespread volcanic activity in the southern Cameroon Line. J. Afr. Earth Sci. 57:96–108

Kenfack PL, Tematio P, Kwekam M, Ngueutchoua G, Njike PR (2011) Evidence of Miocene volcano-sedimentary lithostratigraphic sequence at Ngwa (Dschang Region. West Cameroon): preliminary analyses and geodynamic interpretation. J Pet Technol Altern Fuels 2:25–34

Kettanah YA, Armstrong-Altrin JS, Mohammad FA (2021) Petrography and geochemistry of siliciclastic rocks of the Middle Eocene Gercus Formation, northern Iraq: Implications for provenance and tectonic setting. Geol J 56:2528–2549

Kwékam M, Hartmann G, Njanko T, Tcheumenak KJ, Fozing EM, Njonfang E (2015) Geochemical and isotope Sr-Nd character of Dschang biotite granite: implications for the Pan-African continental crust evolution in West-Cameroon (Central Africa). Earth Sci Res 4(1):88–102

Le Bas MJ, Le Maitre RW, Streckeisen A, Zanettin B (1986) A chemical classification of volcanic rocks based on the total alkali-silica diagram. J Petrol 27(3):745–750

Lowe DR (1982) Sediment gravity flows: II. Depositional models with special reference to the deposits of high-density turbidity currents. J Sedimentary Petrol 52:279–297

Madhavaraju J, Armstrong-Altrin JS, Pillai RB, Pi-Puig T (2021) Geochemistry of sands from the Huatabampo and Altata beaches. Gulf of California. Mexico. Geol J 56(5):2398–2417

Marzoli A, Piccirillo EM, Renne PR, Bellieni G, Iacumin M, Nyobe JB, Tongwa AT (2000) The Cameroon volcanic line revisited: petrogenesis of continental basaltic magma from lithospheric and asthenospheric mantle source. J Petrol 1:87–109

Maurin JC, Guiraud R (1993) Basement control in the development of the Early Cretaceous. West and Central African rift system. Tectonophys 228:81–95

McDonough WF, Sun SS (1995) The composition of the Earth. Chem Geol 120:223–253

McLennan SM (2001) Relationships between the trace element compositions of sedimentary rocks and upper continental crust. Geochem Geophys Geosyst 2:86–98

Mendes AC, Dantas AB, Ribeiro ACS, Santos LO, Mendes KC, Moraes DDS, Almeida RM (2020) Provenance of heavy and clay minerals in bottom sediments of Green Lake, an Amazonian fluvial lake in Brazil. Acta Amazon 1–12. https://doi.org/10.1590/1809-4392201804681

Miall AD (1996) The Geology of fluvial deposits: sedimentary facies, basin analysis and petroleum geology. Springer-Verlag

Miall AD (1978) Lithofacies types and vertical profile models in braided river deposits: a summary. In: Miall, A.D., Ed., fluvial sedimentology. Memoir: Canadian Society of Petroleum Geologists 5. pp 597–604.

Mongelli G, Critelli S, Perri F, Sonnino M, Perrone V (2006) Sedimentary recycling provenance and paleo-weathering from chemistry and mineralogy of Mesozoic continental redbed mudrocks Peloritani Mountains Southern Italy. Geochem J 40:197–209

Montigny R, Ngounouno I, Deruelle B (2004) Ages K-Ar des roches magmatiques du fossé de Garoua (Cameroun): leur place dans le cadre de la «Ligne du Cameroun». Compt Rendus Geosci 336:1463–1471

Moreau C, Regnoult JM, Deruelle B, Robineau B (1987) A new tectonic model for the Cameroon Line. Central Africa Tectonophysics 141:317–334

Nagarajan R, Armstrong-Altrin JS, Kessler FL, Hidalgo-Moral EL, Dodge-Wan D, Taib NI (2015) Provenance and tectonic setting of Miocene siliciclastic sediments. Sibuti Formation. Northwestern Borneo Arab J Geosci 8:8549–8565

Ndjeng E (1992) Etudes de la sédimentation et du modèle d'évolution géodynamique de deux bassins du Crétacé inférieur du Nord-Cameroun: Babouri-Figuil et Mayo Oulo-Léré. Université de Yaoundé, Thèse d'Etat

Ndjigui PD, Bayiga EC, Onana VL, Djenabou-Fadil S, Ngono GSA (2019) Mineralogy and geochemistry of recent alluvial sediments from the Ngaye River watershed, northern Cameroon: Implications for the surface processes and Au-PGE distribution. J Afr Earth Sci 150:136–157

Nemec W, Steel RJ (1984) Alluvial and coastal conglomerates: their significant features and some comments on gravelly mass-flow deposits. In: Koster. E.H..Steel. R.J. (Eds.). Sedimentology of gravels and conglomerates. Canadian Society of Petroleum Geologists Memoir 10. pp 1–31

Nesbitt HW, Young GM (1982) Early Proterozoic climates and plate motions inferred from major element chemistry of lutites. Nature 299:715–717

Nesbitt HW, Young GM (1984) Prediction of some weathering trends of plutonic and volcanic rocks based on thermodynamic and kinetic consideration. Geochem Cosmochim Acta 48:1523–1534

Nesbitt HW, Young GM (1989) Formation and diagenesis of weathering profiles. J Geol 97:129–147

Ngangom E (1983) Etude tectonique du fossé crétacé de la Mbéré et du Djerem. Sud-Adamaoua. Cameroun. Bull. Cent. Rech. Explor. Prod. Elf Aquitaine 7(1):339–347

Ngueutchoua G, Ekoa Bessa AZ, Eyong Taken J, Demanou Zandjio D, Djaoro Baba H, Tchami Nfada L (2019) Geochemistry of Cretaceous fine-grained siliciclastic rocks from Upper Mundeck and Logbadjeck formations, Douala sub-basin, SW Cameroon: Implications for weathering intensity, provenance, paleoclimate, redox-condition and tectonic setting. J Afr Earth Sci 152:215–236

Nilsen TH (1982) Alluvial fan deposits. In: Sholle, P.A. Spearing. D. (Eds.). Sandstone depositional environments. American Association of Petroleum Geologists Memoir **31** pp 49–86.

Njike Ngaha PR, Mfayakouo CB, Bitom D (2014) Paleogeographic evolution of the Eastern edge of the Douala Basin from Early Cenomanian to Turonian. Open Geol J 8:124–141

Njike Ngaha PR (1984) Contribution à l'étude géologique, stratigraphique et structurale de la bordure du bassin atlantique au Cameroun. Thèse 3eme cycle. Universite de Yaoundé

Njonfang E, Nono A, Kamgang P, Ngako V, Tchoua MF (2011) Cameroon line alkaline magmatism (Central Africa): A reappraisal. Geol Soc Amer Special Paper 478:173–191

Njonfang E (1998) Contribution à l'étude de la relation entre la "Ligne du Cameroun" et la direction de l'Adamaoua: 1- Pétrologie. Géochimie et structure des granitoïdes Panafricains de la zone de cisaillement Foumban-Bankim (Ouest-Cameroun et Adamaoua). 2- Pétrologie et géochimie des formations magmatiques tertiaires associées. Thèse d'État. Université de Yaoundé 1

Ntamak-Nida MJ, Bourquin S, Makong JC, Baudin F, Mpesse JE, Itjoko Ngouem C, Komguem PB, Abolo GM (2010) Sedimentology and sequence stratigraphy from outcrops of the Kribi-Campo sub-basin: Lower Mundeck formation (Lower Cretaceous, southern Cameroon). J Afr Earth Sci 58:1–18

Parfenoff A, Pomerol Ch, Tourenq J (1970) Les minéraux en grains: Méthodes d'études et détermination. Masson, Paris

Perri F (2014) Composition, provenance and source weathering of Mesozoic sandstones from Western-Central Mediterranean Alpine chains. J Afr Earth Sci 91:32–43

Perri F, Critelli S, Mongelli G, Cullers RL (2011) Sedimentary evolution of the Mesozoic continental redbeds using geochemical and mineralogical tools: the case of Upper Triassic to lowermost Jurassic Monte di Gioiosa Mudrocks (Sicily. Southern Italy). Int J Earth Sci 100:1569–1587

Pletsch T, Erbacher J, Holbourn AEL, Kuhnt W, Moullade M, Oboh-Ikuenobede FE, Soding E, Wagner T (2001) Cretaceous separation of Africa and South America: the view from the West African margin (ODP Leg 159). J South Amer Earth Sci 14:147–174

Prosser G, Bentivenga M, Laurenzi MA, Caggianelli A, Dellino P, Doronzo D (2008) Late Pliocene volcaniclastic products from Southern Apennines: distal witness of early explosive volcanism in the central Tyrrhenian Sea. Geol Mag 145(4):521–536

Ramos-Vazquez MA, Armstrong-Altrin JS (2019) Sediment chemistry and detrital zircon record in the Bosque and Paseo del Mar coastal areas from the southwestern Gulf of Mexico. Mar Petrol Geol 110:650–675

Ramos-Vazquez MA, Armstrong-Altrin JS (2021) Provenance of sediments from Barra del Tordo and Tesoro beaches, Tamaulipas State, northwestern Gulf of Mexico. J Palaeogeogr 10:1–17

Rashid SA, Gana IJA, Masoodi A, Khan FA (2015) Major and trace element geochemistry of lake sediments. India: implications for weathering and climate control. Arab J Geosci 8:10481–10496

Roser BP, Korsch RJ (1986) Determination of tectonic setting of sandstone-mudstone suites using SiO₂ content and K₂O/Na₂O ratio. J Geol 94:635–650

Roser BP, Korsch RJ (1988) Provenance signatures of sandstone-mudstone suites determined using discrimination function analysis of major element data. Chem Geol 67:119–139

Tawfik HA, Salah MK, Maejima W, Armstrong-Altrin JS, Abdel-Hameed AMT, El Ghandour MM (2017) Petrography and geochemistry of the Lower Miocene Moghra sandstones. Qattara Depression, north Western Desert. Egypt. Geol J 1–16.

Taylor SR, McLennan SM (1985) The Continental crust: its composition and evolution. Blackwell Scientific, Oxford

Tchouatcha MS (2011) Les bassins du Mbere et du Djerem dans le contexte régional Sud Adamaoua: genèse, évolution stratigraphique et reconstitution des paléoenvironnements. Université de Yaoundé, Thèse de Doctorat Ph.D, p 1

Tchouatcha MS, Njike Ngaha PR, Mahmoud MS, Deaf AS, Ekodeck GE (2010) Existence of "late continental" deposits in the Mbere and Djerem sedimentary basins (north Cameroon): palynologic and stratigraphic evidence. J Geol Mining Res 2(6):159–169

Tchouatcha MS, Azinwi Tamfuh P, Kemteu Sobdjou C, Mbesse CO, Ngnotue T (2021a) Provenance, palaeo-weathering and depositional environment of the Cretaceous deposits from the Babouri-Figuil and Mayo Oulo-Lere basins (North-Cameroon) during the Southern Atlantic opening: Geochemical constraints. J Afr Earth Sci 174.https://doi.org/10.1016/j.jafrearsci.2020.104052

Tchouatcha MS, Kouske AP, Deaf AS, Mioumnde AP (2021b) Geochemical, mineralogical and sedimentological analyses of reworked sediments (new) in the syn- to post-rift Middle Cretaceous-Quaternary detrital deposits from western Atlantic margin of Cameroon: evidence from sedimentation-erosion alternation in the context of passive margin evolution. Acta Geochim. https://doi.org/10.1007/s11631-021-00455-5

Velde B (1992) Introduction to clay mineral. Chemistry, origin, uses and environmental significance. Chapman and Hall

Verma SP, Armstrong-Altrin JS (2013) New multi-dimensional diagrams for tectonic discrimination of siliciclastic sediments and their application to Precambrian basins. Chem Geol 355:117–133

White AF, Blum AE (1995) Effects of climate on chemical weathering in watersheds. Geochem Cosmochim Acta 59:1729–1747

Yan DT, Chen DZ, Wang QC, Wang JG (2010) Large-scale climate fluctuations in the latest Ordovician on the Yangtze block, south China. Geol 38:599–602

Youmen D, Schmincke HU, Lissom J, Etame J (2005) Données géochronologiques: mise en evidence des différentes phases volcaniques au miocène dans les Monts Bambouto (Ligne du Cameroun). Sci Technol Dev 11:49–57

Zaid SM (2015) Geochemistry of sands along the Ain Soukhna and Ras Gharib beaches. Gulf of Suez. Egypt: Implications for provenance and tectonic setting. Arab J Geosci 8:10481–10496

Zeng S, Wang J, Chen W, Fu X, Feng X, Song C, Wang D, Sun W (2019) Geochemical characteristics of early Cretaceous marine oil shale from Changshe Mountain area in the northern Qiangtang Basin. Tibet: implication for palaeo-weathering, provenance, tectonic setting and organic matter accumulation. Geol J 1–18. https://doi.org/10.1002/gj.3579

Zhou L, Friis H, Poulsen MLK (2015) Geochemical evaluation of the Late Paleocene and Early Eocene shales in Siri canyon. Danish-Norwegian Basin Mar Petrol Geol 61:111–122

Zou S, Wu C, Xu D, Shan Q, Zhang X, Hollings P (2016) Provenance and depositional setting of Lower Silurian siliciclastic rocks on Hainan Island. South China: implications for a passive margin environment of South China in Gondwana. J Asi Earth Sci 123:243–262